

# Demonstration of infrared nBn photodetectors based on the AlInAsSb digital alloy materials system <sup>F</sup>

Cite as: Appl. Phys. Lett. **119**, 031101 (2021); <https://doi.org/10.1063/5.0058462>

Submitted: 30 May 2021 . Accepted: 02 July 2021 . Published Online: 19 July 2021

Dekang Chen, Renjie Wang, J. Andrew McArthur, Xingjun Xue, Andrew H. Jones, Seth R. Bank, and  Joe C. Campbell

## COLLECTIONS

 This paper was selected as Featured



View Online



Export Citation



CrossMark

## ARTICLES YOU MAY BE INTERESTED IN

[Current-induced magnetization switching at charge-transferred interface between topological insulator \(Bi,Sb\)<sub>2</sub>Te<sub>3</sub> and van der Waals ferromagnet Fe<sub>3</sub>GeTe<sub>2</sub>](#)

Applied Physics Letters **119**, 032402 (2021); <https://doi.org/10.1063/5.0057863>

[Temperature dependence of the picosecond spin Seebeck effect](#)

Applied Physics Letters **119**, 032401 (2021); <https://doi.org/10.1063/5.0050205>

[Low noise Al<sub>0.85</sub>Ga<sub>0.15</sub>As<sub>0.56</sub>Sb<sub>0.44</sub> avalanche photodiodes on InP substrates](#)

Applied Physics Letters **118**, 081106 (2021); <https://doi.org/10.1063/5.0035571>

 QBLOX



1 qubit

Shorten Setup Time

**Auto-Calibration**  
**More Qubits**

Fully-integrated

**Quantum Control Stacks**  
**Ultrastable DC to 18.5 GHz**  
Synchronized <<1 ns  
Ultralow noise



100s qubits

[visit our website >](#)

# Demonstration of infrared nBn photodetectors based on the AlInAsSb digital alloy materials system

Cite as: Appl. Phys. Lett. **119**, 031101 (2021); doi: [10.1063/5.0058462](https://doi.org/10.1063/5.0058462)

Submitted: 30 May 2021 · Accepted: 2 July 2021 ·

Published Online: 19 July 2021



View Online



Export Citation



CrossMark

Dekang Chen,<sup>1</sup> Renjie Wang,<sup>1</sup> J. Andrew McArthur,<sup>2</sup> Xingjun Xue,<sup>1</sup> Andrew H. Jones,<sup>1</sup> Seth R. Bank,<sup>2</sup> and Joe C. Campbell<sup>1,a)</sup> 

## AFFILIATIONS

<sup>1</sup>Department of Electrical and Computer Engineering, University of Virginia, Charlottesville, Virginia 22904, USA

<sup>2</sup>Microelectronics Research Center, University of Texas, Austin, Texas 78758, USA

<sup>a)</sup>Author to whom correspondence should be addressed: [jcc7s@virginia.edu](mailto:jcc7s@virginia.edu)

## ABSTRACT

We report an nBn photodetector based on the AlInAsSb digital alloy materials system, which has the advantage of a near-zero valence band offset. These photodetectors have achieved 28% external quantum efficiency, dark current densities of  $2.6 \times 10^{-3}$  A/cm<sup>2</sup> at 300 K and  $1.8 \times 10^{-9}$  A/cm<sup>2</sup> at 100 K with  $-0.5$  V bias, and detectivity of  $1.7 \times 10^{10}$  Jones at room temperature under  $2 \mu\text{m}$  wavelength illumination.

Published under an exclusive license by AIP Publishing. <https://doi.org/10.1063/5.0058462>

Photodetectors that operate in the mid-wave infrared (MWIR) spectral range are of growing interest for applications in sensing<sup>1</sup> and imaging.<sup>2</sup> The n-barrier-n (nBn) structure significantly reduces Shockley–Read–Hall (SRH) generation currents, which is particularly beneficial for MWIR detection owing to the requisite narrow bandgap absorbers.<sup>3</sup> As a result, compared with other midwave infrared detectors, such as p-i-n photodiodes, the nBn photodetectors achieve lower dark current and lower noise, which enables higher operating temperatures and improved signal-to-noise performance. An nBn photodetector usually consists of a narrow bandgap undepleted, n-type absorber followed by a wide bandgap barrier layer. The large conduction band offset at the barrier layer effectively blocks the diffusion of majority carriers (electrons) but allows minority carriers (holes) to pass through. Since the nBn photodetector operates with low voltage across the narrow bandgap absorber, the SRH generation and tunneling are moderated to a great extent. It is also beneficial that the Fermi level is not near mid-gap in these devices. In PIN diodes, the mid-gap Fermi level in the intrinsic region leads to SRH generation, which is usually the biggest noise source in cooled detectors.

To date, substantial progress has been made with nBn photodetectors fabricated from a wide range of materials, including the InAs/GaSb type-II superlattice (T2SL)<sup>3,4</sup> and the InAs/InAsSb type-II strained layer superlattice (T2SLS).<sup>5,6</sup> Compared to the T2SL, the T2SLS is easier to grow<sup>7</sup> and has longer minority carrier lifetimes.<sup>8</sup> However, the quantum efficiency of T2SLS nBn photodetectors at a

long-wave infrared (LWIR) range is limited by the low absorption coefficients,<sup>9,10</sup> especially in n-type absorbers,<sup>11</sup> due to the longer superlattice period of the T2SLS.<sup>10,12</sup> While effort toward enhancing T2SLS quantum efficiency and reducing dark current is ongoing,<sup>12,13</sup> another promising approach lies in new materials' systems that have the potential to overcome the intrinsic limitations of conventional superlattices. Recently, high performance avalanche photodiodes (APDs) have been demonstrated in the  $\text{Al}_x\text{In}_{1-x}\text{As}_y\text{Sb}_{1-y}$  (referred to as AlInAsSb) digital alloy material system.<sup>14–17</sup> These devices show high gain, low dark current, extremely low excess noise, and high temperature stability compared to conventional III-V materials. AlInAsSb is also a promising candidate for MWIR nBn photodetectors with the unique characteristic of a minimal valence band discontinuity within a wide range of bandgap energies (from 0.247 to 1.3 eV).<sup>18,19</sup> This eliminates hole trapping at the absorber/barrier valence band discontinuity, giving rise to longer hole diffusion length, higher quantum efficiency, lower turn-on voltage, and higher detectivity.

AlInAsSb is a short-period super-lattice structure composed of four binary alloys.<sup>20</sup> The target wavelength for the nBn photodetector reported here was chosen to be  $2 \mu\text{m}$ , where high performance AlInAsSb APDs have been previously demonstrated.<sup>17</sup> Figure 1 shows a schematic cross section of the AlInAsSb structure. The absorber is  $\text{Al}_{0.3}\text{InAsSb}$  ( $E_g = 0.58$  eV), and the barrier is  $\text{Al}_{0.7}\text{InAsSb}$  ( $E_g = 1.16$  eV). XPS characterization indicates that the AlInAsSb materials system has near-zero valence band discontinuity.<sup>18</sup> Therefore, the conduction band offset

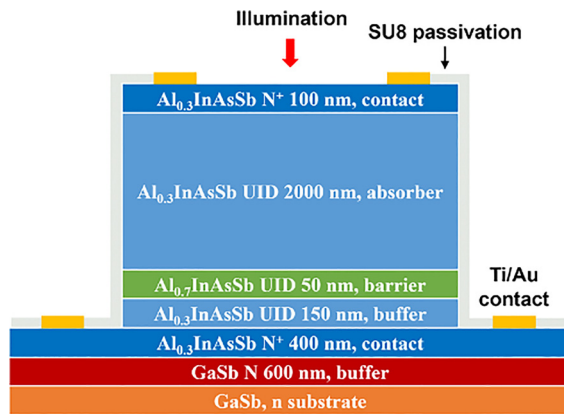


FIG. 1. Schematic cross section of the AlInAsSb nBn photodetector.

should be approximately the bandgap difference between  $\text{Al}_{0.3}\text{InAsSb}$  and  $\text{Al}_{0.7}\text{InAsSb}$ , i.e., 0.58 eV, which is sufficient to suppress the thermionic emission of majority carriers over the barrier. The active layers (absorber, barrier, and buffer layer) were sandwiched by two highly doped N  $\text{Al}_{0.3}\text{InAsSb}$  contact layers. A buffer layer was inserted beneath the barrier layer to avoid possible dopant diffusion from the N contact layer. The band diagram has been modeled using a Lumerical CHARGE solver<sup>21</sup> and is plotted in Fig. 2 at equilibrium (a), under reverse bias (b), and under forward bias (c).

Two of the primary design parameters are the thickness and the doping concentration of the absorber. Since the nBn photodetector has very low electric field applied across the absorber, the photocurrent is primarily a diffusion current. A thicker absorber will achieve higher absorption; however, collection of the photogenerated carriers may be limited by the diffusion length.<sup>22</sup> Figure 3(a) shows the simulated absorption and responsivity vs the absorber thickness. While the absorption increases with thickness, the responsivity peaks and then decreases for thickness greater than  $\sim 3 \mu\text{m}$ . The reason for this behavior is revealed by the simulated carrier collection efficiency shown in Fig. 3(b). Below an absorber thickness of  $2 \mu\text{m}$ , the increase in the carrier collection efficiency is due to more light being absorbed in the absorber than in the buffer layer where electrons are blocked by the wide bandgap barrier layer. Above  $2 \mu\text{m}$ , the collection efficiency decreases due to the diffusion-length limitation. As a result, there is an

optimum thickness that balances these opposing effects, which in this case is  $\sim 3 \mu\text{m}$ .

The doping concentration in the absorber affects the depletion width, electric field, carrier lifetime, and the dark current.<sup>9,23</sup> Figure 4 shows the simulated responsivity of the device with different n-type doping concentrations in the  $\text{Al}_{0.3}\text{InAsSb}$  absorber and the buffer layer. The barrier layer is unintentionally doped. The responsivity decreases as the doping concentration increases, which is primarily due to the decreased depletion width when the doping concentration in the absorber is high. As a result, the electric field intensity will be higher on one side, which will give rise to SRH recombination and tunneling, and a decreased responsivity as a result of reduced carrier lifetime. High n-type doping may also decrease the carrier lifetime of holes through band-to-band recombination in the undepleted region. Therefore, a lower doping concentration in the absorber and buffer layers is preferred and is designed to be unintentionally doped. For the device reported here, the n-type background doping concentration was approximately  $1 \times 10^{16} \text{ cm}^{-3}$ . Modifying the doping polarity and concentration in the barrier layer has been reported to minimize the valence band discontinuity, so as to increase the hole diffusion length and reduce the turn-on voltage.<sup>23,24</sup> However, since AlInAsSb has minimal valence band discontinuity, the barrier layer doping was not considered.

The structure shown in Fig. 1 was grown by MBE as a digital alloy of three binary constituents: AlSb, InAs, and InSb lattice matched to an n-type GaSb substrate.<sup>20</sup> Devices were fabricated into circular mesa structures by citric acid wet etching using standard photolithography techniques, and SU-8 was used for surface passivation. Finally, current-voltage (I-V), capacitance-voltage (C-V), external quantum efficiency (EQE), and low-temperature dark current measurements were performed to characterize the performance of the device.

Figure 5(a) shows the room-temperature I-V characteristics of the AlInAsSb nBn photodetector. The photoresponse is measured under  $2\text{-}\mu\text{m}$  laser illumination. The dark current density is  $\sim 2.6 \times 10^{-3} \text{ A/cm}^2$  at  $-0.5 \text{ V}$  and  $\sim 2.7 \times 10^{-3} \text{ A/cm}^2$  at  $-1 \text{ V}$ . Based on the I-V measurement, the detectivity was determined from  $1/RA$  to be  $1.7 \times 10^{10}$  Jones at room temperature. It also worth noting that the forward dark current is lower than the reverse dark current at low bias but shows a faster rise with bias. This can be understood by comparing Figs. 2(b) and 2(c). Due to the asymmetric design of the nBn photodetector, the buffer layer is much thinner than the absorber. Therefore,

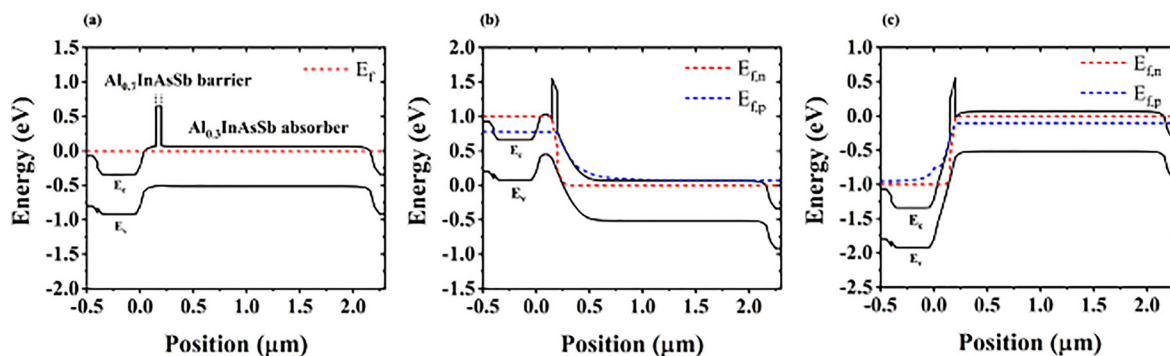
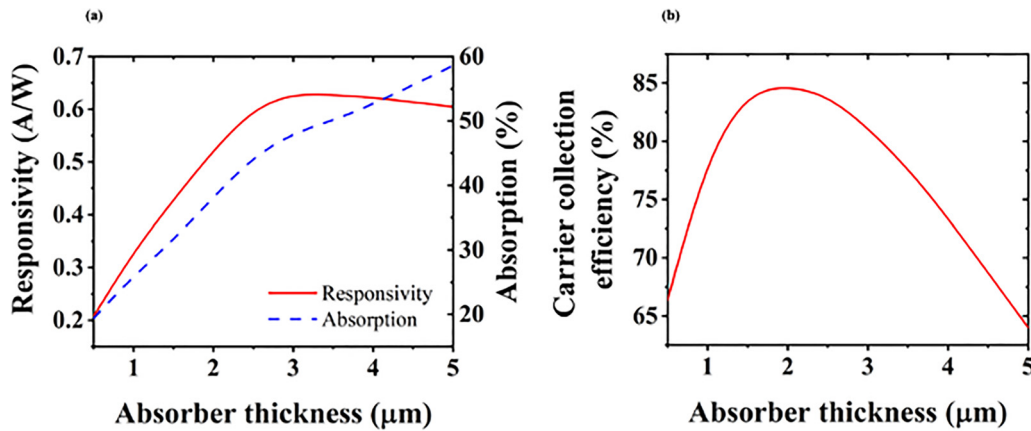
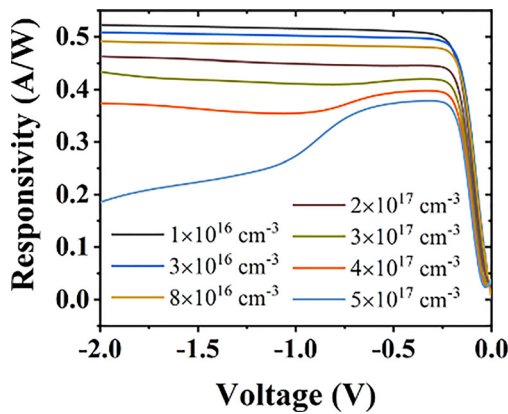


FIG. 2. Simulated energy band diagram of the AlInAsSb nBn photodetector (a) at equilibrium, (b) under a reverse bias of  $-1 \text{ V}$ , and (c) under a forward bias of  $1 \text{ V}$ .



**FIG. 3.** (a) Simulated responsivity and absorption and (b) carrier collection efficiency of the AlInAsSb nBn photodetector vs absorber thickness under 2- $\mu\text{m}$  illumination. The absorber, the barrier, and the buffer layer are assumed to be unintentionally doped with an n-type background doping concentration of  $1 \times 10^{16} \text{ cm}^{-3}$ ; the simulation temperature is 300 K.



**FIG. 4.** Simulated responsivity vs voltage of the AlInAsSb nBn photodetector with different n-type doping concentrations in the absorber and the buffer layer.

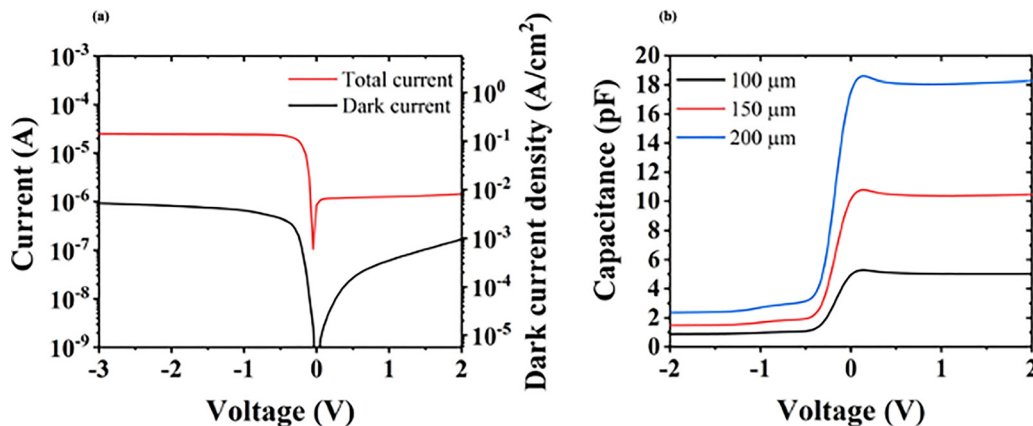


**FIG. 5.** (a) Measured I-V curves of a 150- $\mu\text{m}$  diameter AlInAsSb nBn photodetector at room temperature; total current was measured under 2- $\mu\text{m}$  laser illumination. (b) Measured C-V curves of AlInAsSb nBn photodetectors with different mesa diameters.

at a low bias, the forward dark current, determined by the thin buffer layer, should be lower than the reverse dark current, determined by the thick absorber. However, as shown in Fig. 2(c), the depletion is confined in the thin buffer layer even when the forward bias increases. As a result, the electric field is high, which finally leads to a rapid increase in the SRH-generated dark current. This trend is consistent with the C-V measurement shown in Fig. 5(b), where the forward capacitance is much higher than the reverse capacitance, which is caused by the narrower depletion width under forward bias.<sup>25</sup> Similarly, the forward photocurrent is also lower than the reverse photocurrent since the majority of the light is absorbed in the thick absorber but the generated photocarriers are blocked by the barrier layer.

Figure 6(a) shows the measured room-temperature EQE. The device exhibits a cutoff wavelength of  $\sim 2.1 \mu\text{m}$ , consistent with the previous work on 2- $\mu\text{m}$  AlInAsSb APDs using the same absorber material.<sup>17</sup> The fast decrease in the EQE around 2  $\mu\text{m}$  should be primarily due to the decreasing absorption coefficient as the photon energy approaches the bandgap energy of  $\text{Al}_{0.3}\text{InAsSb}$ , which is similar

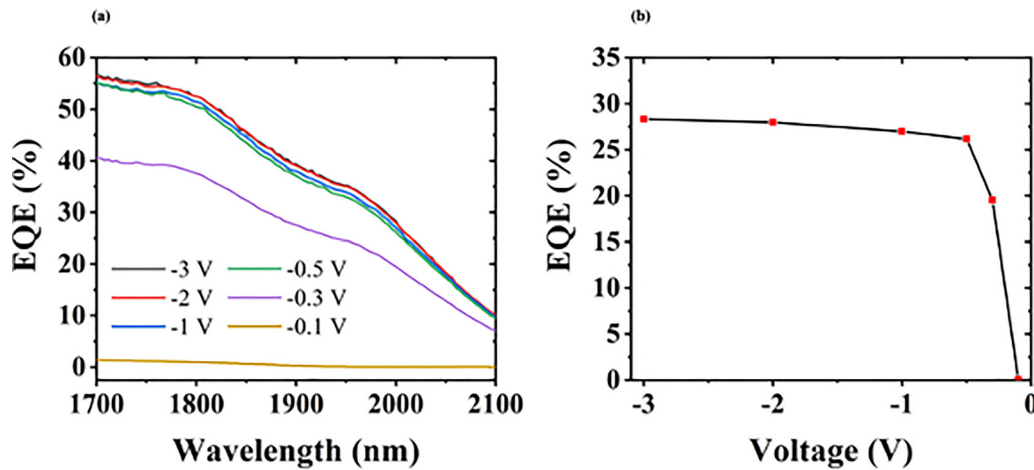


FIG. 6. (a) Room temperature measured EQE of a 250- $\mu\text{m}$  diameter AlInAsSb nBn photodetector vs wavelength for a reverse bias from  $-0.1$  to  $-3$  V. (b) EQE at 2  $\mu\text{m}$  vs reverse bias voltage.

to the behavior of T2SL near cutoff.<sup>26</sup> The saturated EQE at 2- $\mu\text{m}$  is  $\sim 28\%$ , close to the simulated EQE of  $\sim 32\%$ . We note that there is no anti-reflection (AR) coating on the device surface. Since the top  $\text{Al}_{0.3}\text{InAsSb}$  layer should have a reflectivity of  $\sim 31\%$  at 2  $\mu\text{m}$ ,<sup>27</sup> the EQE could be increased to  $\sim 40\%$  with a 1%-reflectivity AR coating. Moreover, by comparing the simulation shown in Fig. 3, the EQE could also be further enhanced by increasing the absorber thickness to  $\sim 3$   $\mu\text{m}$ , which with AR coating would yield an EQE of  $\sim 50\%$  at 2  $\mu\text{m}$ .

Figure 6(b) shows a clear turn-on behavior at approximately  $-0.5$  V. This turn-on characteristic reflects the voltage needed to overcome carrier trapping, especially in the valence band.<sup>23</sup> Since AlInAsSb has a minimal valence band discontinuity with different Al compositions, the turn-on characteristic shown here is likely caused by the barrier formed by the interface of the UID buffer layer and the highly doped N contact layer, as shown in Fig. 2(b). This is different

from a conventional nBn detector, where the valence band discontinuity at the barrier layer also plays an important role. The turn-on voltage can be reduced, which will enable zero-bias operation, by modifying the doping concentrations in the contact layer and the buffer layer.

To better compare the dark current of the AlInAsSb nBn detector to conventional nBn detectors, the low temperature dark current was measured in a cryogenic chamber from 80 to 340 K. Figure 7(a) shows the dark current density vs the bias voltage and the dark current density vs the inverse temperature in Fig. 7(b). The dashed line in Fig. 7(b) shows a fit to the diffusion-current-limited regime using the relation

$$J_{\text{diff}} \propto T^3 \exp\left(\frac{-\Delta E}{kT}\right),$$

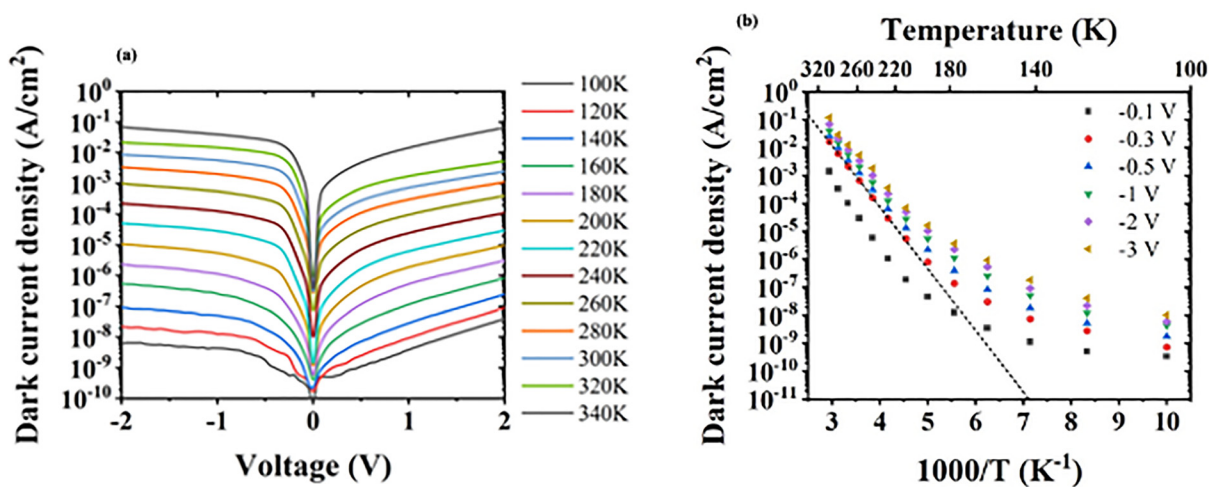


FIG. 7. (a) Measured dark current density of a 150- $\mu\text{m}$  diameter AlInAsSb nBn photodetector at different temperatures. (b) Measured dark current density as a function of the inverse temperature. The dashed line shows the fitting to the diffusion-current-limited regime.

where  $T$  is the temperature,  $k$  is the Boltzmann constant, and  $\Delta E$  is the activation energy. Fitting to this equation reveals background-limited infrared photo-detection (BLIP) temperatures of 180 and 200 K and activation energies of  $\sim 0.41$  and  $\sim 0.37$  eV at  $-0.1$  and  $-0.3$  V, respectively. These activation energies are between  $E_g/2$  (0.29 eV) and  $E_g$  (0.58 eV) of  $\text{Al}_{0.3}\text{InAsSb}$ . For these devices, the mesa was etched down to the bottom contact layer, resulting in a  $2\text{-}\mu\text{m}$  deep sidewall. Compared with conventional nBn photodetectors, where the absorber and barrier layers are usually un-etched or partially un-etched with contact made to the absorber,<sup>12</sup> the observed activation energies are most probably the result of the large sidewall exposure. Hence, a lower dark current can be expected with an etch that does not fully extend through the absorber. While dark current densities lower than those of T2SL<sup>4</sup> and T2SLS<sup>13</sup> nBn detectors are observed, this is due in part to the larger bandgap energy of the  $\text{AlInAsSb}$  absorber. Further research with narrower bandgap  $\text{AlInAsSb}$  absorbers is in progress.

We report  $\text{AlInAsSb}$  digital alloy nBn photodetectors. This material system has the benefit of a near-zero valence band offset, an advantage for nBn detectors. For  $2\text{-}\mu\text{m}$  illumination, the external quantum efficiency is 28%. The dark current densities are  $2.6 \times 10^{-3}$  A/cm<sup>2</sup> at 300 K and  $1.8 \times 10^{-9}$  A/cm<sup>2</sup> at 100 K with  $-0.5$  V bias, and detectivity is  $1.7 \times 10^{10}$  Jones at room temperature.

This work was supported by the Army Research Office and DARPA (Contract No. W911NF-17-1-0065) and DARPA (Contract No. W909MY-12-D-0008) and by the National Science Foundation (Award No. ECCS-1933836).

## DATA AVAILABILITY

The data that support the findings of this study are available from the corresponding author upon reasonable request.

## REFERENCES

- R. Linares, G. Vergara, R. Gutiérrez, C. Fernández, V. Villamayor, L. Gómez, M. González-Camino, and A. Baldasano, in *Proc. SPIE 9485, Thermosense: Thermal Infrared Applications XXXVII*, edited by S. J. (Tony) Hsieh and J. N. Zalameda (Baltimore, Maryland, 2015), p. 94851F.
- F. Prel, L. Moreau, S. Lantagne, R. D. Bullis, C. Roy, C. Vallières, and L. Levesque, *Proc. SPIE 8014, Infrared Imaging Systems: Design, Analysis, Modeling, and Testing XXII* (SPIE, Orlando, FL, 2011), p. 801411.
- J. B. Rodriguez, E. Plis, G. Bishop, Y. D. Sharma, H. Kim, L. R. Dawson, and S. Krishna, *Appl. Phys. Lett.* **91**, 043514 (2007).
- H. J. Lee, H. C. Jung, A. Jang, J. G. Kim, S. Y. Ko, Y. H. Kim, and J. Nah, *Infrared Phys. Technol.* **94**, 161 (2018).
- H. S. Kim, O. O. Cellek, Z. Y. Lin, Z. Y. He, X. H. Zhao, S. Liu, H. Li, and Y. H. Zhang, *Appl. Phys. Lett.* **101**, 161114 (2012).
- K. Michalczewski, P. Martyniuk, L. Kubiszyn, C. H. Wu, Y. R. Wu, J. Jureczyk, A. Rogalski, and J. Piotrowski, *IEEE Electron Device Lett.* **40**, 1396 (2019).
- D. Z. Ting, A. Soibel, A. Khoshkhalagh, S. A. Keo, S. B. Rafol, A. M. Fisher, B. J. Pepper, E. M. Luong, C. J. Hill, and S. D. Gunapala, *Infrared Phys. Technol.* **97**, 210 (2019).
- E. H. Steenbergen, B. C. Connelly, G. D. Metcalfe, H. Shen, M. Wraback, D. Lubyshv, Y. Qiu, J. M. Fastenau, A. W. K. Liu, S. Elhamri, O. O. Cellek, and Y. H. Zhang, *Appl. Phys. Lett.* **99**, 251110 (2011).
- P. C. Klipstein, Y. Livneh, A. Glozman, S. Grossman, O. Klin, N. Snapi, and E. Weiss, *J. Electron. Mater.* **43**, 2984 (2014).
- I. Vurgaftman, G. Belenky, Y. Lin, D. Donetsky, L. Shterengas, G. Kipshidze, W. L. Sarney, and S. P. Svensson, *Appl. Phys. Lett.* **108**, 222101 (2016).
- P. Klipstein, in *SPIE 6940, Infrared Technology and Applications XXXIV*, edited by B. F. Andresen, G. F. Fulop, and P. R. Norton (SPIE, Orlando, FL, 2008), p. 69402U.
- D. Z. Ting, A. Soibel, A. Khoshkhalagh, S. A. Keo, A. M. Fisher, S. B. Rafol, L. Höglund, C. J. Hill, B. J. Pepper, and S. D. Gunapala, *Appl. Phys. Lett.* **118**, 133503 (2021).
- A. Soibel, D. Z. Ting, S. B. Rafol, A. M. Fisher, S. A. Keo, A. Khoshkhalagh, and S. D. Gunapala, *Appl. Phys. Lett.* **114**, 161103 (2019).
- M. E. Woodson, M. Ren, S. J. Maddox, Y. Chen, S. R. Bank, and J. C. Campbell, *Appl. Phys. Lett.* **108**, 081102 (2016).
- A. H. Jones, Y. Yuan, M. Ren, S. J. Maddox, S. R. Bank, and J. C. Campbell, *Opt. Express* **25**, 24340 (2017).
- A. H. Jones, A. K. Rockwell, S. D. March, Y. Yuan, S. R. Bank, and J. C. Campbell, *IEEE Photonics Technol. Lett.* **31**, 1948 (2019).
- A. H. Jones, S. D. March, S. R. Bank, and J. C. Campbell, *Nat. Photonics* **14**, 559 (2020).
- J. Zheng, A. H. Jones, Y. Tan, A. K. Rockwell, S. March, S. Z. Ahmed, C. A. Dukes, A. W. Ghosh, S. R. Bank, and J. C. Campbell, *Appl. Phys. Lett.* **115**, 122105 (2019).
- A. H. Jones, "Al<sub>x</sub>In<sub>1-x</sub>As<sub>y</sub>Sb<sub>1-y</sub> digital alloy avalanche photodiodes for low noise applications," Doctorate dissertation (University of Virginia, Charlottesville, 2020).
- S. J. Maddox, S. D. March, and S. R. Bank, *Cryst. Growth Des.* **16**, 3582 (2016).
- See <https://www.lumerical.com/products/> for "CHARGE: 3D Charge Transport Simulator," Lumerical, Inc.
- S. Maimon and G. W. Wicks, *Appl. Phys. Lett.* **89**, 151109 (2006).
- D. Z. Ting, A. Soibel, A. Khoshkhalagh, and S. D. Gunapala, *Opt. Eng.* **56**, 091606 (2017).
- N. D. Akhavan, G. Jolley, G. A. Umana-Membreno, J. Antoszewski, and L. Faraone, *IEEE Trans. Electron Devices* **62**, 722 (2015).
- A. Glasmann, I. Prigozhin, and E. Bellotti, *IEEE J. Electron Devices Soc.* **7**, 534 (2019).
- H. Katayama, T. Takekawa, M. Kimata, H. Inada, and Y. Iguchi, *Infrared Phys. Technol.* **70**, 53 (2015).
- D. Chen, K. Sun, A. H. Jones, and J. C. Campbell, *Opt. Express* **28**, 24379 (2020).